Queensland University of Technology
Brisbane Australia

This is the author's version of a work that was submitted/accepted for publication in the following source:

Ahtiainen, Juhana, Peynot, Thierry, Saarinen, Jari, & Scheding, Steven (2013) Augmenting traversability maps with ultra-wideband radar to enhance obstacle detection in vegetated environments. In *Proceeding of the 2013 IEEE/RSJ International Conference on Robots and Intelligent Systems*, IEEE, Tokyo Big Sight, Tokyo, pp. 5148-5155.

This file was downloaded from: `http://eprints.qut.edu.au/67656/`

© Copyright 2013 IEEE

Personal use of this material is permitted. Permission from IEEE must be obtained for all other users, including reprinting/ republishing this material for advertising or promotional purposes, creating new collective works for resale or redistribution to servers or lists, or reuse of any copyrighted components of this work in other works.

Notice: *Changes introduced as a result of publishing processes such as copy-editing and formatting may not be reflected in this document. For a definitive version of this work, please refer to the published source:*

http://dx.doi.org/10.1109/IROS.2013.6697101

Augmenting Traversability Maps with Ultra-Wideband Radar to Enhance Obstacle Detection in Vegetated Environments

Juhana Ahtiainen, Thierry Peynot, Jari Saarinen, and Steven Scheding

***Abstract*— Operating in vegetated environments is a major challenge for autonomous robots. Obstacle detection based only on geometric features causes the robot to consider foliage, for example, small grass tussocks that could be easily driven through, as obstacles. Classifying vegetation does not solve this problem since there might be an obstacle hidden behind the vegetation. In addition, dense vegetation typically needs to be considered as an obstacle. This paper addresses this problem by augmenting probabilistic traversability map constructed from laser data with ultra-wideband radar measurements. An adaptive detection threshold and a probabilistic sensor model are developed to convert the radar data to occupancy probabilities. The resulting map captures the fine resolution of the laser map but clears areas from the traversability map that are induced by obstacle-free foliage. Experimental results validate that this method is able to improve the accuracy of traversability maps in vegetated environments.**

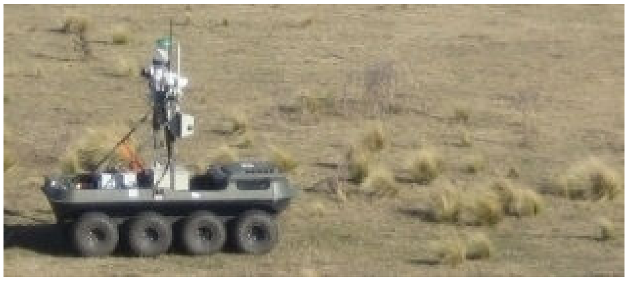

Fig. 1: Multiple grass tussocks in front of the vehicle that are usually seen as obstacles by the LIDAR.

I. INTRODUCTION

Obstacle detection is a critical task for field robots. Most existing systems rely on geometric representation of the environment that is most commonly formed either by using a vision system or a LIDAR. However, when robots are operating on vegetated terrain, the geometric representation may not be sufficient for good navigation performance. Relying solely on geometric representation may force the robot to circumvent vegetation that could easily be driven over, which wastes time and energy. For example, the grass tussocks shown in Fig. 1 could be driven over but LIDAR-based perception systems see them as obstacles. In densely vegetated environments it may not even be possible to reach the goal without traversing through vegetation.

This problem has been partly addressed by classifying vegetation from other types of obstacles. For example, in [1] a multispectral camera is utilised for detecting vegetation based on the fact that chlorophyll strongly absorbs visible light and reflects near-infrared (NIR) light. In [2] and [3] a 3D LIDAR is used to classify grass from other obstacles based on statistical analysis of the 3D data points. However, these methods do not solve the obstacle detection problem since there might be solid obstacles hidden behind the vegetation. This poses a great risk if the robot needs to traverse through this area without any knowledge of what is behind the vegetation.

Sensors operating at high frequencies of the electromagnetic (EM) spectrum, e.g., cameras and LIDARs, cannot provide sufficient information since neither visible light nor infrared light travel through vegetation. UWB radars typically operate at relatively low frequencies and therefore are able to penetrate vegetation [4]. For example, in [5] an impulse radar of $2.2GHz$ was used to detect a tree trunk behind $2.5m$ of branches and foliage.

In this paper, we propose a method for augmenting LIDAR-based traversability maps with UWB radar data such that areas of obstacle-free foliage (an area of vegetation that could be driven through) can be cleared. The resulting augmented traversability map captures the best properties of both sensors by exploiting the fine resolution of the LIDAR and the penetrability of the UWB radar. We analyse the foliage penetrability of the radar as well as study what kind of obstacles the radar is able to detect. We also provide extensive experimental validation of the proposed method with two different platforms and environments. To the best of our knowledge, this is the first paper to propose a method for refining traversability maps with UWB radar measurements with a thorough experimental validation on UGV platforms.

The paper is organised as follows. Section II discusses the related work and Section III describes the proposed approach for augmenting traversability maps with UWB radar data. Section IV presents the experimental system used for validation and outlines implementation details. Section V provides experimental results of the radar calibration process and the obstacle detection tests. Finally, Section VI concludes the paper and discusses future work.

The work was supported in part by the Australian Centre for Field Robotics, the Air Force Research Laboratory under agreement FA2386-10-1-4153, Academy of Finland under project number 115898, and both the Finnish Funding Agency for Technology and Innovation (TEKES) and Forum for Intelligent Machines (FIMA) under Famous project. The U.S. Government is authorized to reproduce and distribute reprints for Governmental purposes notwithstanding any copyright notation thereon.

J. Ahtiainen and J. Saarinen are with Department of Automation and Systems Technology, Aalto University, Finland `firstname.lastname@aalto.fi`

T. Peynot and S. Scheding are with Australian Centre for Field Robotics, University of Sydney, Australia `tpeynot@acfr.usyd.edu.au`, `s.scheding@acfr.usyd.edu.au`

II. RELATED WORK

Occupancy grids [6] are a popular tool for obstacle detection approaches in robotics. A probabilistic occupancy grid [7] divides the environment into equally sized grid cells, whose values are occupancy probabilities. An elevation map is a $2.5D$ grid map capable of representing the height of the cells [8]. LIDARs are popular sensors for constructing grid maps but any kind of range data can be used [9]. In [10] and [11] millimetre-wave (MMW) radars are used to construct probabilistic occupancy grids.

Traversability maps quantify the difficulty a robot would encounter traversing through a particular region and are typically platform dependent [12]. In [13] a traversability index for each grid cell in an elevation map is calculated using the terrain slope and roughness. In [14] a machine learning method was used to learn the traversability of a road ahead using data from LIDAR, camera, and inertial measurement unit (IMU). However, these methods rely on range data from sensors that are not capable of penetrating foliage and therefore see vegetation as obstacles.

Only a few studies use UWB radar for detecting obstacles in vegetated areas. In [15] a ground penetration radar is used to detect obstacles within vegetation as well as underground. In [16] a UWB radar is used to build maps in vegetated environments. In [17] a custom radar array is built to study the possibility to detect obstacles through vegetation. However, this study concentrate only on UWB radar-based obstacle detection and does not address the terrain traversability. In iRobot's DareDevil project [18] a UWB radar is used in parallel with a LIDAR to study all-weather operations. The authors also discuss obstacle detection within vegetation but do not show any experimental results.

The method proposed in this paper utilises a UWB radar to gain more information about the laser-obstacles (obstacles seen by a LIDAR) in vegetated environments. The goal of this study is to be able to reduce the number of laser-obstacles originating from obstacle-free foliage from a LIDAR-based traversability map. This will enable the robot to safely operate in vegetated environments where LIDAR-based obstacle detection is not sufficient.

III. APPROACH

Pulsed UWB radars operate by transmitting and receiving very short duration UWB pulses. These radars return a vector of power measurements of the radar cross-sections (RCS) of targets within the field of view (FOV) [10]. The elements in the vector are range bins. UWB radars typically operate at relatively low frequencies and are therefore able to penetrate some amount of vegetation. The low frequency results in large beamwidth [4], which makes it difficult to capture the real dimensions of obstacles. However, by using an appropriate sensor model and computing a probabilistic occupancy grid, this problem can be mitigated if obstacles are seen from different angles.

The proposed approach of augmenting traversability maps with UWB radar data consists of three separate phases. Firstly, a grid-based traversability map, T_m, is built using LIDAR data. Each cell of this map contains a value of traversability, which quantifies the difficulty of a robot to traverse through that area. Secondly, the traversability map and radar returns are used to compute the adaptive detection thresholds. Finally, a refined grid-based traversability map is computed by fusing UWB radar data with the traversability map.

A. Target Detection Using UWB Radar

UWB radar return vectors can be very noisy, therefore, a detection filter is needed. The popular constant false alarm rate (CFAR) [19] method does not perform well in environments with frequent obstacles or with radars that return short measurement vector. The thresholds presented in [11] cannot be adopted to UWB radars due to different noise characteristics [4].

The detection thresholds utilised in this study are determined by measuring returns from the radar when the whole FOV is traversable according to the T_m. This approach enables adaptation to different kind of surfaces. The area is sampled with the radar and the detection thresholds for each range bin are calculated as the mean of measurements for that range bin. The corresponding detection threshold vector is denoted by T_d.

The ground clutter generates multiple returns exceeding T_d, which is undesirable since clutter measurements should be ignored. On the other hand, sometimes the returns from obstacles can be below T_d. Therefore, also minimum and maximum intensity of the ground returns are calculated for each range bin and used in the sensor model to take account of returns near T_d. This will be discussed below. The minimum and maximum thresholds are denoted by T_{min} and T_{max} respectively. The thresholds are illustrated in Fig. 2(a).

T_{max} is always set to be greater than T_d, such that the occasional clutter measurements do not generate false positives on the map, i.e.,

$$T_{max} = T_d + c_{th}, \quad \text{if} \quad T_{max} - T_d < c_{th}, \tag{1}$$

where c_{th} is experimentally defined constant. $c_{th} = 3$ is used in this study.

In addition to the thresholds, also the shape of the return is exploited. The energy reflected back to the receiver from objects results in peaks in the received signal [20]. Objects with large RCS span multiple range bins exceeding the T_d causing uncertainty in the range of the detection. For example, in 2(a) all the three targets span at least three range bins. Therefore, peaks are also detected from the return vector. For each range bin exceeding T_d, the number of range bins to the closest peak is calculated and the value is used in the sensor model to refine the detection. This will be discussed below.

B. Sensor model

The sensor model converts the radar returns to a probability of individual cells in the FOV of the radar being occupied. An inverse sensor model is used in this study due to computational efficiency. The proposed sensor model is adapted from the prior work done with narrowband radars ([10] and [11]) for UWB radars. The noise characteristics of UWB radars differ from those of narrowband radars and the beamwidth is typically significantly larger [4]. Therefore, we present a probabilistic sensor model specially designed for UWB radars, which also considers the wide FOV and the UWB radar noise.

Given a radar measurement vector, first we limit the measurements that are usable. The maximum measurement range, R_{max}, was determined through extensive testing with a variety of object such that these objects were no longer reliably detectable beyond R_{max}. Due to substantial noise that typically occurs at close range with UWB radars, a minimum distance, R_{min}, is also determined. In this study $R_{max} = 10m$ and $R_{min} = 3.5m$ are used. Only cells between R_{min} and R_{max} are updated.

The transmitted signal attenuates as a function of distance but also from the objects in the FOV that reflect a variable amount of energy back to the receiver. Therefore, it is less probable to correctly detect free space after the first detected object than before. To account for this attenuation, the FOV of the radar is divided into three regions by range where measurement probabilities are calculated differently. These regions are illustrated in Fig. 2.

Every range bin where the measured intensity exceeds T_d is considered a detection. These cells corresponding to detections are members of region r_1. Range bins where the measured intensity is below T_d, are considered to be free of obstacles. These cells corresponding to areas free of obstacles are members of regions r_2 or r_3.

The limiting factor between r_2 and r_3 is the first r_1 region that exceeds T_{max}. The reason for using T_{max} instead of T_d is that ground clutter often exceeds T_d but does not affect the signal attenuation significantly. In addition, real obstacles that cause the intensity to be below T_{max} have small RCS and do not attenuate the signal much. Cells behind the furthest echo are not updated since the last object could be occluding the signal completely.

The measurement likelihood, $P(z|occ)$, of cells belonging to r_1 are updated with

$$P(z|occ) = G_\theta(\alpha) * G_{pw}(z(b)) * G_{pk}(d) * P_O, \qquad (2)$$

where z is the radar return vector. G_θ is an angle scaler, which models the antenna gain pattern. α is the angle between the beam axis and the centroid of the cell in question. G_{pw} is a power scaler, which takes into account the intensity of particular range bin b. G_{pk} is a peak scaler, which refines the range measurement based on the shape of the return. d is the number of bins between the nearest peak and b. It is assumed that these scalers are independent, thus multiplication rule is used to calculate the overall probability. The scalers are discussed in detail below. P_O is a constant that limits the maximum probability. $P_O = 0.8$ is used in this study to account for errors in the model and reduce the effect of transient noise in the measurements. Hence, $P(z|occ)$ is bounded between 0.5 and 0.8.

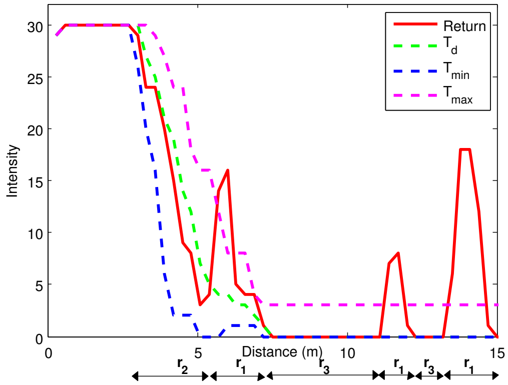

(a) Radar return

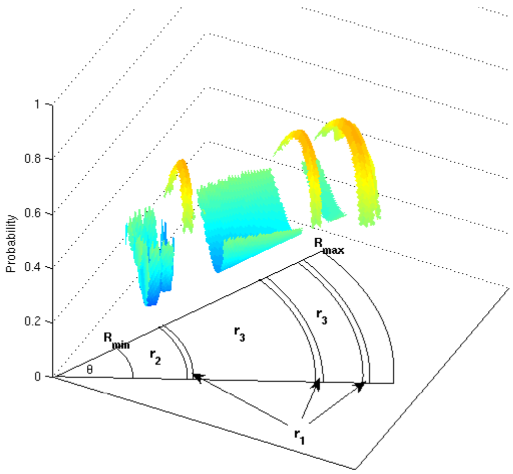

(b) Corresponding probabilities

Fig. 2: (a): A radar return with three targets in the FOV, drawn in red. Detection T_d, minimum T_{min}, and maximum thresholds T_{max} are illustrated with green, blue, and magenta dashed lines respectively. (b): Corresponding occupancy probabilities calculated with the sensor model. θ is the beamwidth, R_{min} and R_{max} are the minimum and maximum detection range respectively.

The region r_2 is the space clear of obstacles before the first detection exceeding T_{max}. The emptiness, $P(z|\neg occ)$, for each cell of this region are calculated with

$$P(z|\neg occ) = G_\theta(\alpha) * G_{pw}(z(b)) * G_d(r) * (1 - P_{C2}), \qquad (3)$$

where G_d is a distance scaler and r is the measured range. $P_{C2} = 0.2$ is a constant that limits the maximum value of $P(z|\neg occ)$ such that it is bounded between 0.5 and 0.8. Selection of P_O and P_{C2} is discussed in V-B.

The region r_3 is clear of obstacles after the first detection exceeding T_{max} but in front of the last detection exceeding T_d. $P(z|\neg occ)$ for each cell of this region are calculated with Eq. (3) except that P_{C2} is replaced with P_{C3} such that $P_{C2} < P_{C3}$. Experimentally defined $P_{C3} = 0.3$ is used in this study.

The scalers in Eq. (2) and Eq. (3) are discussed below:

1) Angle Scaler: The beam pattern is modelled with an inverse parabola which approximates the beam pattern well [10]. Hence, the angle scaler, G_θ, is

$$G_\theta(\alpha) = 1 - \frac{2\alpha^2}{\theta^2}, \tag{4}$$

where α is the angle between beam axis and the centre of the current cell and θ is the beamwidth.

2) Power Scaler: A sigmoid function is used to approximate a probability function

$$G_{pw}(z(b)) = \frac{1}{1 - e^{-\frac{c}{d} z(b)}}, \tag{5}$$

where c is a scaling constant, d is the difference between T_d and T_{max} or T_d and T_{min}, and $z(b)$ is the measured intensity of range bin b. The sigmoid function is scaled such that probability at T_{min} is 0.0067 and at T_{max} 0.9526 which yields the values of the scaling constant $c = 5$ and $c = 3$ respectively. These values were determined experimentally.

3) Peak Scaler: A peak scaler lowers the probability of measurements that exceed T_d but are not peaks in order to refine the detection. This is modelled with a Normal distribution

$$G_{pk_{pdf}}(d) = \frac{1}{\sqrt{2\pi}\sigma} e^{\frac{(-d-\mu)^2}{2\sigma^2}}, \tag{6}$$

where the mean, μ, is the range bin of nearest observed peak, σ is the standard deviation, and d is the number of range bins from the nearest peak to the current range bin. In our implementation we use $\sigma = 4$, which yields that peak scaler completely eliminates measurements that are more than four range bins away from the nearest peak. The peak scaler, G_{pk}, is obtained by scaling the probability of the mean to one.

4) Distance Scaler: The distance scaler G_d is used when calculating measurement probabilities of r_2 and r_3. It models the fact that it is less probable to correctly measure free space as the detection range increases. It scales the distance linearly according to

$$G_d(r) = \frac{R_{max} + R_{min} - r}{2R_{max}} + 0.5, \tag{7}$$

where r is the Euclidean distance from the centroid of the current cell to the radar.

C. Data Fusion

The augmented traversability map, T_{ma}, is initialized with the values from T_m. Only when there is untraversable area in the FOV of the radar according to T_m, the corresponding cells in T_{ma} are updated with radar measurements using the sensor model with Bayes' formula assuming static world and conditional independence [6]. Traversable areas are not updates, since the LIDAR data are less noisy than UWB radar data.

Using this approach, each cell that gets updated with the radar measurements is initialized with high prior probability. This way if the radar does not provide sufficient evidence to clear or confirm the LIDAR observation, the cell remains untraversable.

IV. SYSTEM DESCRIPTION

This section presents the experimental system used for validation and discusses the implementation of the proposed approach.

A. UWB radar

The UWB radar used in this study is called Radar Developer's Kit Lite (RaDeKL) and it is manufactured by Multi Spectral Solutions Inc (MSSI). The radar performance characteristics are presented in Table I.

TABLE I: Technical specifications of RaDeKL UWB radar

RF Characteristics	
Centre Frequency	6.35 GHz
Bandwidth	400 Mhz (-3 dB)
Peak Power	50 mW EIRP
Antenna gain	12 dBi w/4x4 Array
Antenna FOV	40 deg AZ x 40 deg EL
System Performance	
Range Extent	256 range bins w/variable offsets
Range resolution	30 cm
Parameters	
Transmit Attenuation (Tx)	0 dB
Receive Attenuation (Rx)	0 dB

B. Measurement platforms

The measurement platforms, Shrimp and Argo, can be seen in Fig. 3. Shrimp is based on Segway's Robotic Mobile Platform RMP-400 and Argo is an 8 wheel skid-steering vehicle. Both platforms are equipped with a Novatel SPAN System (Synchronized Position Attitude and Navigation) with a Honeywell IMU positioning system, which usually provides $2cm$-accuracy localisation estimates. In addition to the UWB radar and the positioning system, the SICK LMS 291 LIDARs indicated in Fig. 3 are used in this study.

C. Implementation

A traversability map, T_m, required by the proposed approach is calculated with the method in [13]. First, an elevation map is calculated from LIDAR returns. Traversability index, τ, is then calculated for each cell using the slope and roughness of the terrain.

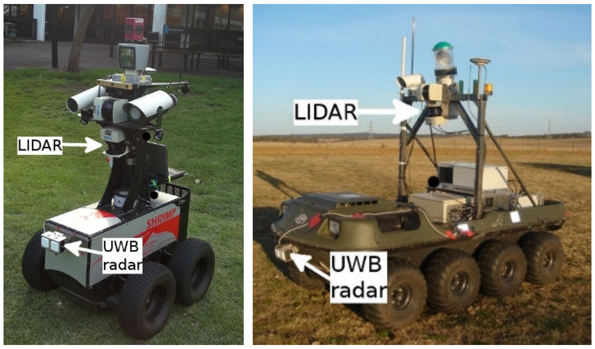

(a) Shrimp (b) Argo

Fig. 3: The measurement platforms used for validation. Exteroceptive sensors used in this study are marked on the pictures.

The resulting T_m is converted to occupancy values by dividing the τ of each cell by a platform-specific untraversability constant, $T_i = 40$. Every cell with a τ above T_i is considered untraversable and the values below are scaled between 0 and 1.

V. EXPERIMENTAL RESULTS

The Subsection V-A shows the RCS of different obstacles as seen by the UWB radar. It also shows the attenuation of the signal with different amount of vegetation in front of a target. Subsection V-B demonstrates the performance of the overall algorithm proposed in this study in three different field trials.

A. *Obstacle Detection with UWB Radar*

First, we tested the detectability of various objects without vegetation. Metal, plastic, wood, and stone obstacles were placed $10m$ in front of the radar and the reflectivity of these obstacles can be seen in Fig. 4. The thresholds T_m, T_{min}, and T_{max} are also illustrated in the figure and $P(z|occ)$ for each target is calculated using these thresholds and the sensor model assuming that the targets are in the middle of the FOV. $P(z|occ)$ along with the dimensions and the RCS of each target are presented in Table II. The RCS values are estimated based on calculated RCS of the radar reflectors using the method in [10].

TABLE II: Properties of different targets

Obstacle	RCS	Dimensions	$P(z\|occ)$
Metal Jerry	8.6 m^2	34 x 45 x 13 cm	0.8000
Large reflector	7.3 m^2	25 x 25 x 25 cm	0.8000
Plastic Jerry	2.6 m^2	32 x 45 x 14 cm	0.7999
Plywood	2.3 m^2	34 x 36 x 2 cm	0.7996
3 bricks	1.5 m^2	23 x 33 x 7 cm	0.7950
2 bricks	0.2 m^2	29 x 17 x 7 cm	0.5346
Stone	0.1 m^2	40 x 20 x 30 cm	0.4606
Cardboard box	N/A	28 x 23 x 24 cm	0.4606

The cardboard box and the stone could not be detected $10m$ away from the radar. Hence, the $P(z|occ)$ for these targets is below 0.5. On the other hand, the RCS of cardboard box could not be estimated since the box does not reflect anything back to the radar. The RCS of the stone was estimated using data from closer range. The column of two bricks is detected $10m$ away from the radar, but the return is weak, which results in small $P(z|occ)$. All the other targets are detected clearly and the corresponding $P(z|occ)$ is large.

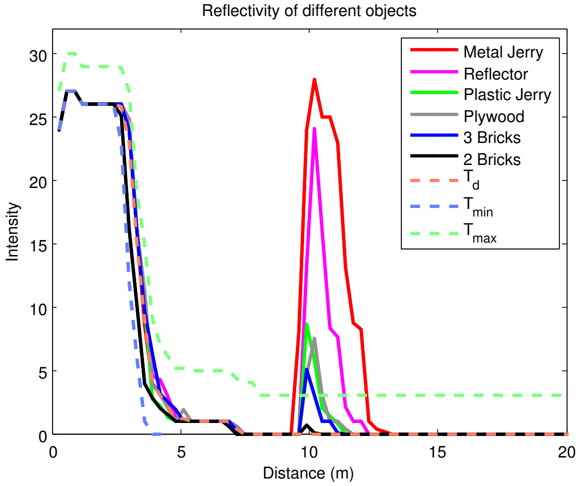

Fig. 4: Reflectivity of different obstacles.

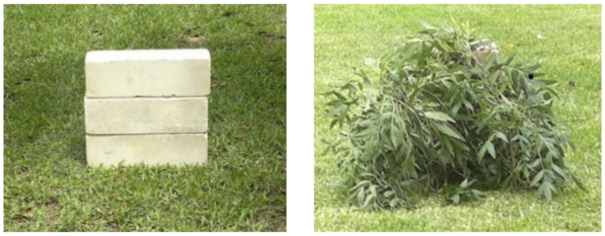

(a)

(b)

Fig. 5: (a) A column of three bricks. (b) two layers of vegetation in front of the bricks.

In the second experiment, the effects of vegetation were tested by progressively placing branches of an Ash tree (Fraxinus Excelsior) and Eucalyptus (Eucalyptus obliqua) in front of a column of three bricks. The radar signal penetrability is illustrated in Fig. 6 with T_m, T_{min}, and T_{max}. The intensities are not directly comparable to those in Fig. 4 since different radar parameters were used. The column of three bricks was placed $9m$ in front of the radar and vegetation was added $1m$ in front of the bricks layer by layer. In Fig. 5(b) two layers of vegetation can be seen with a column of three bricks behind the foliage. Each layer adds approximately $10cm$ of foliage.

From the Fig. 6 it is clear that the return signal attenuates as vegetation is added. Four or more layers of vegetation are dense enough to reflect the signal back to the radar such that the vegetation is considered as an obstacle. However, with four layers some amount of the radiation still penetrates the vegetation and the bricks are detected. With five layers of vegetation the bricks are no longer detected. The measured intensity of the vegetation is smaller than with four layer due to scattering of the signal.

B. *Field Trials*

Three field trials were conducted; the first two in a controlled environment on relatively flat lawn and the third in a rural environment with numerous grass tussocks on the test area. The test sites are shown in Fig. 7.

Four different experiments were performed in the Trial 1. In experiment a, the area was clear of obstacles, then, in experiment b, obstacles were added (small reflector, stone, two-brick column and three-bricks column). For experiment c, branches of an ash tree were added in front of the obstacles and on a clear spot on the lawn such that it was hardly possible to see anything visually behind the foliage. In the experiment d the obstacles were completely covered with the branches, i.e., not detectable behind vegetation by the the human eye.

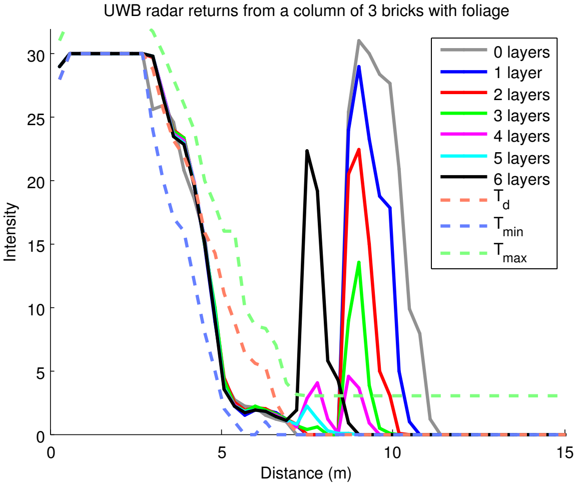

Fig. 6: Radar returns from 3 bricks $9m$ away from the radar with different amount of vegetation $1m$ in front of them.

In the Trial 2, a total of six different experiments were performed. In experiment a, the lawn was clear of obstacles and three obstacles (i.e., 2 bricks, 3 bricks, and a stone) were added for the experiment b. Then, branches of Eucalyptus tree were added layer by layer in front of the obstacles as well as on two clear spots on the lawn for experiments c, d, e, and f. One layers was added before each experiment, every layer adding approximately $10cm$ of foliage.

Examples of the resulting T_m from Trials 1 and 2 are shown in Fig. 8(a) and 8(d). The locations of the obstacles are indicated in the figures. Corresponding T_{ma} are shown in Fig. 8(c) and Fig. 8(f). Fig. 8(b) and 8(e) indicate how long each cell that was updated with the radar data spent in the FOV of the radar during the experiment.

Table III summarises the results from the first two trials. The same numbers cannot be calculated for the third trial since the ground truth is not known. The most important numbers in this case are false negative rate (FNR) and true negative rate (TNR), since we are interested in clearing areas from T_m. TNR is the proportion of cleared obstacle-free foliage cells of all obstalce-free foliage cells. FNR is the proportion of falsely cleared obstacle cells of all obstacle cells. In addition, true negatives (TN), false negatives (FN), true positives (FP), and false positives (FP) are presented. A good description of these terms can be found in [21].

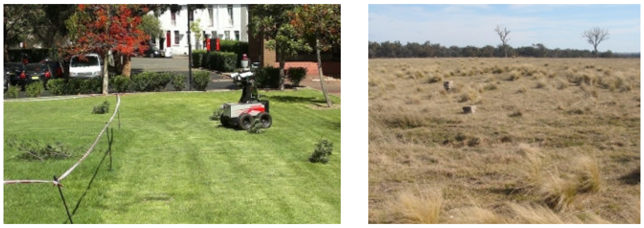

(a) Test site of Trials 1 and 2 (b) Test site of Trial 3

Fig. 7: Photographs from the test sites. The temporary fence seen in Fig. 7(a) was removed in Trial 2.

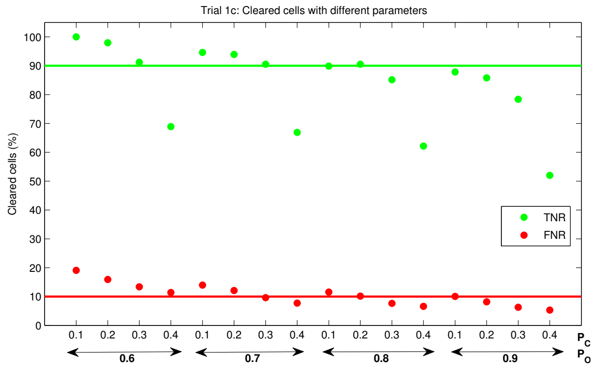

Fig. 9: The effect of parameters P_O and P_{C2}. P_{C3} is set to be 0.1 greater that P_{C2}.

TABLE III: Cleared cells from Trials 1 and 2

	Foliage			Obstacles		
	TN	FP	TNR	FN	TP	FNR
Trial 1						
a) Empty	0	0	N/A	40	556	6.71 %
b) Obstacles	0	0	N/A	125	1398	8.21 %
c) sparse	105	11	90.52 %	312	2928	9.63 %
d) dense	128	20	86.49 %	126	1203	9.48 %
Trial 2						
a) Empty	0	0	N/A	141	1931	6.81 %
b) Obstacles	0	0	N/A	304	1668	15.42 %
c) 1 layer	105	13	88.98 %	182	1936	8.59 %
d) 2 layers	123	16	88.49 %	356	1667	17.60 %
e) 3 layers	117	39	75.00 %	236	1466	13.87 %
f) 4 layers	134	70	65.69 %	208	1797	10.37 %

These values are calculated based on hand labelling foliage and obstacles on the T_m using information of the obstacle locations and size without the foliage. Only the set of cells that have been in the radar FOV more than $2s$ are accounted for in the calculations.

The parameters used in these calculations are $P_O = 0.8$, $P_{C2} = 0.2$, and $P_{C3} = 0.3$. Fig. 9 demonstrates the effects of these parameters in Trial $1c$. It can be seen that TNR and FNR are strongly correlated, which makes selecting the parameters a trade-off between effective foliage clearance and conservative approach. The selected parameters give a good compromise such that more than 90% percent of foliage and only around 10% of the obstacles are cleared.

In Trial $1c$, the area of obstacle-free foliage was cleared completely but in Trial $1d$ a small fraction still remains on the T_{ma}. In every experiment some amount of the foliage around the obstacles was not cleared due to range inaccuracies in the radar measurements. All obstacles were visible on T_{ma} in each experiment. In Trial 2, the column of two bricks or the stone was falsely cleared in experiments b, d, and e, which can be seen in the larger FNR values. This is due to the small RCS of these targets and the slightly different trajectories between experiments.

The TNR values are near 90% in most of the experiments. However, when the amount of vegetation increases, the TNR starts to drop, which is logical since the radar is no longer able to distinguish between foliage and obstacles.

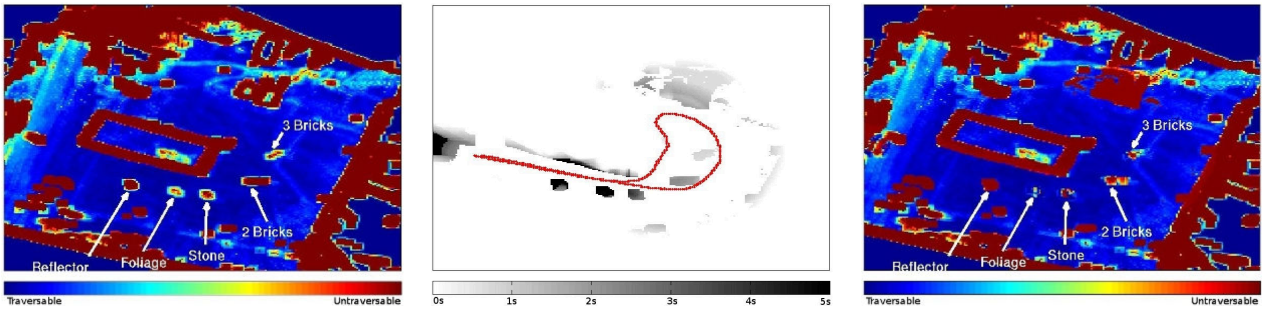

(a) LIDAR Traversability map (T_m)
(b) Updated cells in radar FOV
(c) Augmented traversability map (T_{ma})

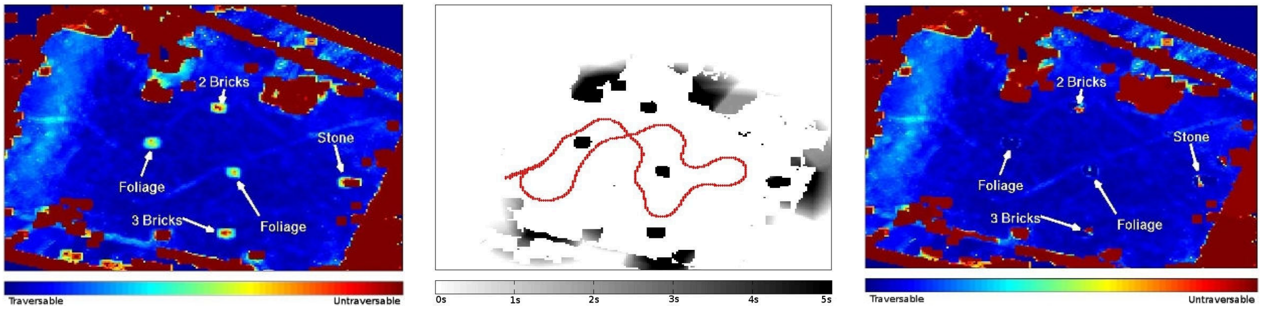

(d) LIDAR Traversability map (T_m)
(e) Updated cells in radar FOV
(f) Augmented traversability map (T_{ma})

Fig. 8: Trial $1d$ on top row and Trial $2c$ on the bottom row. (a) and (d) show the LIDAR traversability maps, coloured by traversability value (red means obstacle); (b) and (e) show the cells that were actually observed by the radar as well, with an intensity of grey proportional to the time spent by the cell in the radar FOV (darker means longer time); (c) and (f) show the augmented occupancy map, coloured by probability values, (blue for 0, red for 1). The size of the test area is around $30 \times 30m^2$.

The FNR values are typically below 10%. There are three reasons that increase the FNR values. Firstly, the range resolution of the radar is $30cm$ and it is not always able to capture the real dimensions of objects, thus some pixels on the edges of obstacles are falsely cleared. Secondly, the annotation is based on traversability map which sometimes exaggerates the size of the objects. Finally, the RCS of some of the obstacles is too small for the radar to detect them reliably and in some experiments they are falsely cleared.

The Trial 3 was conducted in a rural environment with multiple grass tufts and three brick piles (heights: 2, 3, and 4 bricks) on the test area. In addition, there was a small ditch and a car on the area. Maps of Trial 3 can be seen in Fig. 10.

Trial 3 demonstrates that the algorithm works well in a rural environment with numerous grass tussocks in the area. Most of the obstacle-free foliage is cleared from the augmented map along the vehicle trajectory. For example, based on the T_m in Fig. 10(a), it is not possible to plan a route from point A to point B indicated in the map. However, using the corresponding T_{ma}, planning a route between these points is feasible.

VI. CONCLUSIONS

A method for augmenting traversability maps with UWB radar data has been proposed in this paper for generating more realistic traversability maps in vegetated environments. A probabilistic sensor model was developed to convert the radar measurements to occupancy probabilities of individual cells. It was shown that by augmenting LIDAR-based traversability maps with UWB radar data, it is possible to clear obstacle-free foliage from the traversability map. This is especially important in densely vegetated environments where it may be impossible to operate safely without sensors that are able to penetrate foliage. The results from Trials 1 and 2 show that around 90% of the foliage can be cleared in most of the experiments. When the amount of foliage increases, it becomes more difficult to clear the false positives. The results from Trial 3 demonstrate that the presented algorithm works well also in rural environments where LIDAR-based obstacle detection is not sufficient.

However, the radar signal is too noisy to reliably distinguish targets with small RCS from foliage. The RCS of the column of two bricks and the stone proved to be too small for the radar to detect them reliably. Therefore, these obstacles were falsely cleared in some of the experiments.

The radar has relatively high centre frequency and it is not able to penetrate dense vegetation. This is acceptable for smaller vehicles that should not travel through dense vegetation. However, if the algorithm is to be applied to larger vehicles, a radar with lower centre frequency needs to be utilised. In addition, the beamwidth of the radar is large for mapping purposes, which means that multiple observations of the same locations from different point of views are highly recommended. In our current experimental set-up, i.e., with one radar mounted in a fixed position, this requires the robot to effectively scan the environment. Therefore, mounting the radar on a pan-tilt unit or using an array of radars would enhance the accuracy of the approach.

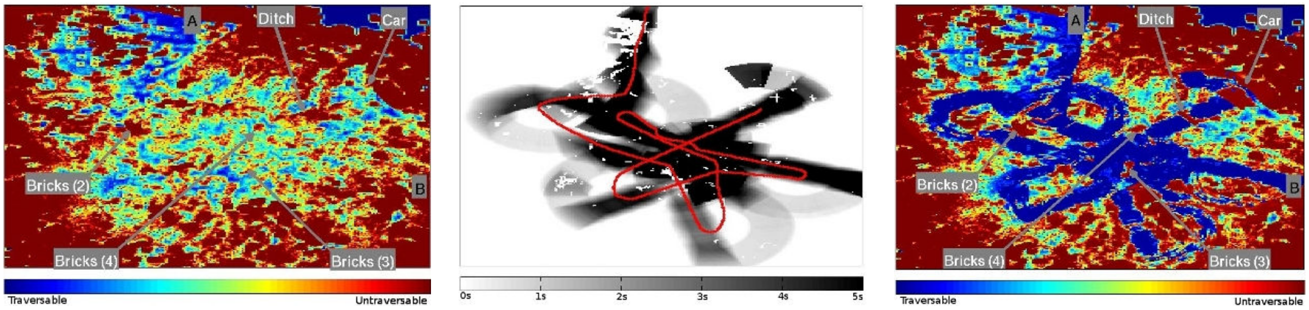

(a) LIDAR Traversability map (T_m)

(b) Updated cells in radar FOV

(c) Augmented traversability map (T_{ma})

Fig. 10: Trial 3: (a) shows the LIDAR traversability map, coloured by traversability value (red means obstacle); (b) shows the cells that were actually observed by the radar as well, with an intensity of grey proportional to the time spent by the cell in the radar FOV (darker means longer time); (c) shows the augmented occupancy map, coloured by probability values, (blue for 0, red for 1). The size of the test area is around $50 \times 50m^2$.

The current implementation of the proposed algorithm does not work in real time. However, no heavy computations are involved and by using 3D LIDAR data, implementing a real-time version of the algorithm should be possible and will be considered in future work.

ACKNOWLEDGMENT

We thank Doug Warwick for providing vegetation, Peter Morton and Zhe Xu for their help with the platforms, Mark Calleija for mouting the radar, and Yannick Godin for photographs and data logging.

REFERENCES

[1] D. Bradley, S. Thayer, A. Stentz, and P. Rander, “Vegetation detection for mobile robot navigation,” Robotics Institute, Carnegie Mellon University, Tech. Rep., 2004.

[2] A. Castano and L. Matthies, “Foliage discrimination using a rotating ladar,” in *Proc. of IEEE Int. Conf. on Robotics and Automation*, Taipei, Taiwan, 2003.

[3] J. Macedo, R. Manduchi, and L. Matthies, “Laser-based discrimination of grass from obstacles for autonomous navigation,” in *Proc. of Int. Sym. on Experimental Robotics*, Honolulu, HI, 2000.

[4] J. Taylor, *Introduction to ultra-wideband systems*. Florida: CRC Press LLC, 2000.

[5] L. Matthies, C. Bergh, A. Castano, J. Macedo, and R. Manduchi, “Obstacle detection in foliage with ladar and radar,” in *Proc of Int. Sym. Laboratory Research*, Sienna, Italy, 2003.

[6] H. Moravec and A. E. Elfes, “High resolution maps from wide angle sonar,” in *Proc. of IEEE Int. Conf. on Robotics and Automation*, Nagoya, Japan, 1985.

[7] H. Moravec, “Sensor fusion in certainty grids for mobile robots,” *AI Magazine*, vol. 9, no. 2, 1998.

[8] B. Siciliano and O. Khatib, *Springer Handbook of Robotics*. Springer, 2008.

[9] S. Thrun, W. Burgard, and D. Fox, *Probabilistic Robotics (Intelligent Robotics and Autonomous Agents)*. The MIT Press, 2005.

[10] A. Fossels, “Scene modelling from motion-free radar sensing,” Ph.D. dissertation, Robotics Institute, Carnegie Mellon University, 2002.

[11] B. Clarke, S. Worrall, G. Brooker, and E. Nebot, “Sensor modelling for radar-based occupancy mapping,” in *Proc. of IEEE/RSJ Int. Conf. on Intelligent Robots and Systems*, Vilamoura, Portugal, 2012.

[12] V. Molino, R. Madhavan, E. Messina, A. Downs, S. Balakirsky, and A. Jacoff, “Traversability metrics for rough terrain applied to repeatable test methods,” in *Proc. IEEE/RSJ Int. Conf. on Robotics and Automation*, 2007.

[13] C. Ye and J. Borenstein, “T-transformation: a new traversability analysis method for terrain navigation,” in *Proc. of the SPIE Defense and Security Sym., Unmanned Ground Vehicle Technology VI*, Orlando FL, 2004.

[14] M. Montemerlo, S. Thrun, H. Dahlkamp, and D. Stavens, “Winning the DARPA grand challenge with an AI robot,” in *Proc. of AAAI National Conf. on Artificial Intelligence*, Boston, MA, 2006.

[15] A. Boryssenko, “Preventing damage by hidden objects in vegetation,” *IEEE Aerospace and Electronic Systems*, vol. 21, no. 12, 2006.

[16] Y. Godin, “Vegetation perception for autonomous vehicles,” BE Thesis, The University of Sydney, 2008.

[17] S. Sun, B. Cho, G. C. Park, Y. S. Kang, and S. Han, “UWB forward imaging radar for an unmanned ground vehicle,” in *Proc. of Int. Asia-Pacific Conf. on Synthetic Aperture Radar*, Seoul, Korea, 2011.

[18] B. Yamauchi, “Fusing ultra-wideband radar and LIDAR for small UGV navigation in all-weather conditions,” in *Proc. of SPIE Vol. 7692 (DS117): Unmanned Systems Technology XII*, Orlando, FL, 2010.

[19] H. Rohling, “Radar CFAR thresholding in clutter and multiple target situations,” *IEEE Transactions on Aerospace and Electronic systems*, vol. 19, no. 4, 1983.

[20] G. Brooker, *Introduction to Sensors for Ranging, and Imaging*. Raleigh, NC: SciTech Publishing, 2009.

[21] T. Fawcett, “An introduction to ROC analysis,” *Pattern Recognition Letters*, vol. 27, no. 8, 2006.